In-situ mineralization of biomass-derived hydrogels boosts capacitive electrochemical energy storage in free-standing 3D carbon aerogels

Achazhiyath Edathil, Anjali; Rezaei, Babak; Almdal, Kristoffer; Keller, Stephan Sylvest

Published in:
Energy & Environmental Materials

Link to article, DOI:
10.1002/eem2.12591

Publication date:
2024

Document Version
Publisher's PDF, also known as Version of record

RESEARCH ARTICLE

Energy & Environmental Materials WILEY

Supercapacitors

In Situ Mineralization of Biomass-Derived Hydrogels Boosts Capacitive Electrochemical Energy Storage in Free-Standing 3D Carbon Aerogels

*Anjali Achazhiyath Edathil, Babak Rezaei, Kristoffer Almdal, and Stephan Sylvest Keller**

Here, a novel fabrication method for making free-standing 3D hierarchical porous carbon aerogels from molecularly engineered biomass-derived hydrogels is presented. In situ formed flower-like $CaCO_3$ molecularly embedded within the hydrogel network regulated the pore structure during in situ mineralization assisted one-step activation graphitization (iMAG), while the intrinsic structural integrity of the carbon aerogels was maintained. The homogenously distributed minerals simultaneously acted as a hard template, activating agent, and graphitization catalyst. The decomposition of the homogenously distributed $CaCO_3$ during iMAG followed by the etching of residual CaO through a mild acid washing endowed a robust carbon aerogel with high porosity and excellent electrochemical performance. At 0.5 mA cm^{-2}, the gravimetric capacitance increased from 0.01 F g^{-1} without mineralization to 322 F g^{-1} with iMAG, which exceeds values reported for any other free-standing or powder-based biomass-derived carbon electrodes. An outstanding cycling stability of ~104% after 1000 cycles in 1 M $HClO_4$ was demonstrated. The assembled symmetric supercapacitor device delivered a high specific capacitance of 376 F g^{-1} and a high energy density of 26 W h kg^{-1} at a power density of 4000 W kg^{-1}, with excellent cycling performance (98.5% retention after 2000 cycles). In combination with the proposed 3D printed mold-assisted solution casting (3DMASC), iMAG allows for the generation of free-standing carbon aerogel architectures with arbitrary shapes. Furthermore, the novel method introduces flexibility in constructing free-standing carbon aerogels from any ionically cross-linkable biopolymer while maintaining the ability to tailor the design, dimensions, and pore size distribution for specific energy storage applications.

1. Introduction

The development of three-dimensional (3D) hierarchical porous carbon structures ranging from macroscopic carbonized monoliths to microscopic carbon nanomaterials is attracting a great degree of interest for energy storage and environmental applications.[1–4] Specifically, these hierarchical carbons possess a unique 3D network with a well-interconnected hierarchical porous structure in terms of macropores (>50 nm), mesopores (2–50 nm), and micropores (<2 nm) that are more beneficial than carbon materials with simple or dual pore structures. The minimized diffusive resistance of mass transport through macropores and larger accessible surface area with effective dispersion of active sites on macro-, meso-, and micropore channels make them attractive as electrode materials for various electrochemical applications.[5,6] However, most hierarchical carbon materials are obtained in powder form, which requires the use of insulating binders (e.g., polytetrafluoroethylene and polyvinylidene fluoride) and a current collector (nickel foams or metal foils). These components occlude significant fractions of the carbon surface and induce increased internal resistance, high electrical and mass transfer resistance, blocked active sites, and undesirable side reactions during the electrochemical process. In addition, they add to the electrode's dead mass and may not maintain good structural integrity during repeated mechanical deformation. Therefore, significant research efforts have been paved to develop free-standing hierarchical porous carbon electrodes in order to significantly reduce weight and bulk volume, resulting in lightweight, low-cost, high-performing electrodes that integrate excellent electrical/ion conductivity, good mechanical strength, and high electrochemical activity.[7–10]

Traditionally, free-standing hierarchically porous carbon materials with well-developed pore structures are fabricated through the sol–gel process of organic precursors (e.g. phenolic resins such as resorcinol formaldehyde) followed by freezing, freeze-drying, and carbonization process (temperature ranging from 400–1000 °C) in an inert atmosphere or through the well-established hydrothermal carbonization.[9,10] This approach results in the formation of macroscopic, milli/centimeter-sized monolithic carbon aerogel (CA) materials with high pore volume and wide pore size distribution. In addition,

Dr. A. A. Edathil, Prof. B. Rezaei, Prof. S. S. Keller
National Centre for Nano Fabrication and Characterization, DTU Nanolab, Technical University of Denmark, 2800, Lyngby, Denmark
E-mail: suke@dtu.dk
Prof. K. Almdal
DTU Chemistry, Technical University of Denmark, 2800, Lyngby, Denmark
The ORCID identification number(s) for the author(s) of this article can be found under https://doi.org/10.1002/eem2.12591.

DOI: 10.1002/eem2.12591

conventional pore-forming approaches such as a subsequent post-treatment involving a second thermal processing step such as physical (steam, CO_2) or chemical (KOH, NaOH, $ZnCl_2$) methods of activation, hard/soft templates, acid etching, air calcination, etc. are performed to introduce hierarchical porosity in the CA.[11] Though the properties and microstructure of hierarchical porous CA could be adjusted at the nanoscale during the fabrication process, the practical development of this approach is hindered by the use of expensive, unsustainable petroleum-derived precursors, complex synthesis routes under harsh environmental conditions, and additional post-activation process. To address this issue, the utilization of biopolymers extracted from biomass as precursors (e.g., polysaccharides, proteins, sugars) to synthesize free-standing hierarchical porous biomass-derived CA (BCA) has attracted broad research interests.[12,13] Aqueous gelation of biopolymers to form hydrogels, which are self-standing water-swollen 3D polymer networks obtained via physical or chemical cross-linking, followed by drying and carbonization in an inert atmosphere, has been demonstrated as a facile route for preparing BCA with 3D monolithic architectures.[6,14,15] Their high availability, low cost, non-toxic nature, environmental friendliness, and stability comply with the requirements typically needed to be used as electrode materials in the most widespread electrochemical applications. However, their poor mechanical property hardly satisfies the requirements for them to be used as free-standing electrodes.

To date, only a few works have been reported on the synthesis of free-standing hierarchical porous BCA from sustainable precursors, which have mainly used polysaccharide-based biopolymers such as bacterial cellulose,[16–18] chitosan,[19] cotton,[20] lignin,[21] and sucrose.[22] These works exploit the use of post-activation treatments using chemicals such as KOH, H_3PO_4, $ZnCl_2$, etc., to improve the interconnectivity of the porous network by creating additional micro- and mesoporosities, which is beneficial for efficient ionic diffusion resulting in extraordinary electrochemical performance. Unfortunately, these corrosive chemicals etch away most carbon and disintegrate the inherent 3D structure, leading to concomitant loss of structural integrity and transforming the free-standing aerogel precursors into powdered CA. These challenges further limit practical application as free-standing electrodes.[23] Therefore, an inexpensive, facile, one-step, and environmentally friendly approach combining the advantages of different renewable carbon precursor materials and activating agents is highly desirable for constructing free-standing hierarchical porous CA electrode materials.

Herein, we report the fabrication of alginate-derived free-standing hierarchically porous 3D carbon aerogels with molecularly engineered active sites for capacitive electrochemical energy storage without the need for an additional post-activation treatment using KOH. This was achieved via a novel strategy introduced as in situ mineralization-assisted one-step activation graphitization (iMAG), as illustrated in **Scheme 1**. Unlike the conventional method for the synthesis of alginate-based semi-interpenetrating polymer network (semi-IPN) hydrogels using H_2O as a solvent (Scheme 1—top row), the proposed method utilized alkaline KOH solution as the biopolymer dissolution media (Scheme 1—bottom row). This, when combined with the $CaCl_2$ cross-linker, enabled the in situ formation of $CaCO_3$ minerals molecularly distributed within the ionic cross-linked hydrogel network, resulting in in situ mineralized biomass-derived aerogel (iMBA) after freezing and freeze-drying. By adjusting the concentrations of KOH used for biopolymer dissolution and $CaCl_2$ as a cross-linker for alginate, the interfacial contact between the carbon precursors (alginate and pullulan), cross-linking Ca^{2+} ions and the in situ formed mineral component $CaCO_3$ was increased. During subsequent iMAG at elevated temperatures of 900 °C, the enclosed $CaCO_3$ minerals acted as a hard template, porogen, activating agent, and graphitization catalyst, successfully transforming the iMBA into a lightweight, compositionally engineered, mechanically robust, free-standing, and binder-free in situ mineralized biomass-derived carbon aerogel (iMBCA). More importantly, during this simultaneous activation and graphitization, the sturdy network formed from the assembly of in situ formed minerals molecularly distributed within the semi-IPN network infuses excellent mechanical strength into the aerogel, thereby maintaining its intrinsic structural integrity and stability. The iMBCA were subjected to mild acid etching (iMBCA-E), removing the minerals in the 3D carbon matrix and increasing the porosity of the CA. Compared to the method without in situ mineralization (BCA-E), this resulted in a unique 3D conductive network with an integrated multiscale carbon structure containing macro/meso/micropores and displaying a high degree of graphitization. The iMBCA-E, when utilized as electrode material for supercapacitors, showed high specific capacitance (322 F g^{-1}), good stability, and a long lifespan with capacitance retention of 104% after 1000 cycles, exceeding the performance of previously reported free-standing BCA. Thus, the introduced iMAG approach provides a facile and eco-friendly strategy for fabricating free-standing hierarchical porous CA from ionically cross-linkable biopolymers with engineered active sites and high structural integrity for various high-performance electrochemical applications.

2. Results and Discussion

2.1. 3D Mold-Assisted Solution Casting of in Situ Mineralized Biomass-Derived Hydrogels

As a first step for the on-demand fabrication of free-standing and electrically conductive carbon aerogels with well-defined shapes and sizes without compromising on mechanical strength, 3D printing-driven mold-assisted solution casting (3DMASC) was established as a novel method for the preparation of in situ mineralized biomass-derived hydrogels (iMBH). As inherent alginate hydrogels possess poor gel rigidity, here, we proposed a robust alginate-based semi-IPN hydrogel with pullulan as the second polymer interlaced in a cross-linked alginate network. Pullulan is a polysaccharide biopolymer produced by Aureobasidium pullulans in starch and sugar cultures and has high aqueous solubility. The 3DMASC process for manufacturing free-standing mineralized hydrogels was demonstrated by filling stereolithography (SLA) 3D printed master molds (Figure S1, Supporting Information) with homogeneous aqueous alkaline (1.0 M KOH) alginate and pullulan solution containing 1.5 and 10 wt.%, respectively (Mineralized route in Scheme 1). The use of alkaline KOH as dissolution media ensured the molecular dispersion of K^+ and OH^- ions within the biopolymer blend. After spraying of $CaCl_2$, iMBH was formed. The diffusion of Ca^{2+} ions caused the spontaneous self-assembling of alginate molecules into an egg-box structure through ionic cross-linking, leaving pullulan interconnected within the alginate network via other non-covalent interactions. Furthermore, the presence of pullulan enabled the formation of alginate/pullulan semi-IPN hydrogels with good structural integrity and mechanical properties. Most

importantly, as seen from Movie S1, Supporting Information, during ionic gelation with 1 M $CaCl_2$, the OH^- ions molecularly dispersed within the alginate/pullulan matrix reacted with Ca^{2+} ions to form $Ca(OH)_2$, which readily absorbs CO_2 from the air to form calcium carbonate ($CaCO_3$) particles within the iMBH network in the first couple of minutes according to the reactions presented in **Equations 1** and **2**.[24]

$$2KOH + CaCl_2 \rightarrow Ca(OH)_2 + 2KCl \quad (1)$$

$$Ca(OH)_2 + CO_2 \rightarrow CaCO_3 + H_2O \quad (2)$$

Notably, the concentration of KOH used for the dissolution of the biopolymers and the agitation or stirring time used for mixing played a crucial role in forming iMBH. The effective dissolution of alginate/pullulan polymer was achieved only when the polymers were mixed in a KOH solution of up to a concentration of 1 M with a stirring time of 3 h. Prolonged mixing favored the degradation of the alginate by the alkaline KOH, resulting in a hydrogel with poorer mechanical properties. Furthermore, utilizing a KOH solution with a concentration higher than 1 M resulted in a monomer solution that failed to gelate during ionic cross-linking with $CaCl_2$. After initial spray cross-linking, the hydrogels were immersed in 1 M $CaCl_2$ for 30 min to ensure complete cross-linking and in situ formation of flower-like $CaCO_3$ hierarchical microstructures within the hydrogel network. Figure S2, Supporting Information, shows the photographs of iMBH, wherein the in situ formed $CaCO_3$ templates turn the gel into white compared to the transparent pristine BH formed using DI water as dissolution media.

2.2. 3D Free-Standing in-Situ Mineralized Biomass-Derived Aerogels

As a next step of the iMAG process, the cross-linked iMBH were detached from the mold, water-washed to remove unreacted Ca^{2+} ions, frozen in dry ice, and subsequently lyophilized. Digital photographs of the resulting free-standing iMBA are presented in **Figure 1a**. For comparison, BA was fabricated similarly but using deionized water as the biopolymer dissolution media instead of an alkaline KOH solution (Non-mineralized route in Scheme 1). Following freeze-drying, a 3D porous framework with micrometer-sized voids corresponding to 90% of its volume was formed in the as-prepared free-standing iMBA due to the removal of the water adsorbed onto the surface of alginate and pullulan macromolecules during hydrogel preparation. Scanning electron microscopy (SEM) images reveal that iMBA (Figure 1b) had a rough surface and a well-interconnected porous 3D network compared to BA (Figure 1e), exhibiting a more uniform surface with very few pores. Moreover, the high-magnification SEM image of iMBA (Figure 1d) revealed that the surface had a well-defined hierarchical morphology, implying the existence of flower-like $CaCO_3$ microcrystals in the polymer network. In contrast, both the cross-section of iMBA (Figure 1c) and BA (Figure 1f) displayed a homogeneous well-stacked flake-like internal structure with a smooth surface, confirming the isotropic diffusion of the cross-linker through the hydrogel. However, the cross-section of iMBA (Figure 1c) further demonstrated the presence of a highly porous 3D network with dense microstructures throughout the aerogel.

The chemical composition of BA and iMBA, including the evolution of $CaCO_3$ microstructures in iMBA was confirmed by X-ray powder

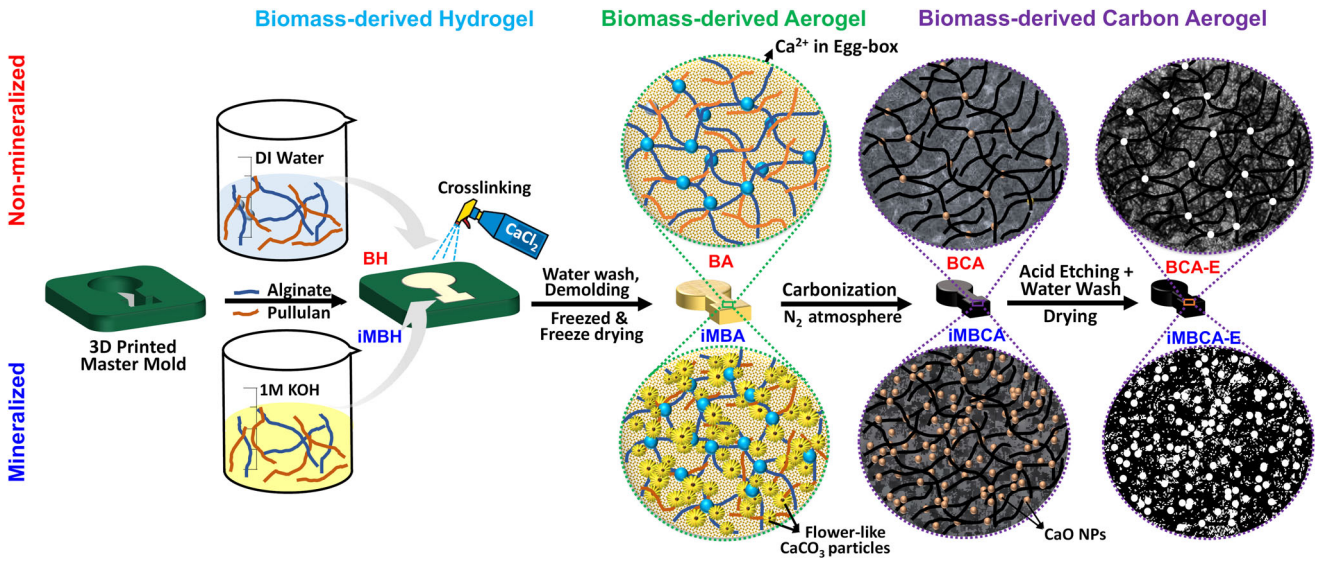

Scheme 1. Schematic diagram for the preparation of free-standing hierarchical porous 3D carbon aerogel electrodes without and with the iMAG strategy. Top row: Synthesis of biomass-derived carbon aerogels (BCA) without mineralization. BH—biomass-derived hydrogels formed by dissolution of alginate and pullulan in deionized water and $CaCl_2$-induced gelation in a 3D printed mold; BA—biomass-derived aerogels obtained after demolding, freezing, and freeze-drying; BCA—carbon aerogels formed during a high-temperature carbonization process under an inert atmosphere; BCA-E—3D carbon electrode after mild acid etching step using 1 M hydrochloric acid (HCl) followed by water wash. Bottom row: Synthesis of BCA using novel iMAG method with mineralization. iMBH—mineralized biomass-derived hydrogels prepared using KOH solution for in situ formation of $CaCO_3$ porogen molecularly distributed within the polymer network; iMBA—in situ mineralized biomass-derived aerogels after freezing and freeze-drying; iMBCA—in situ mineralized carbon aerogels after one-step self-activation of in situ formed $CaCO_3$ particles combined with graphitization; iMBCA-E: Highly porous biomass-derived 3D carbon aerogel electrode after etching of the remaining minerals and water wash.

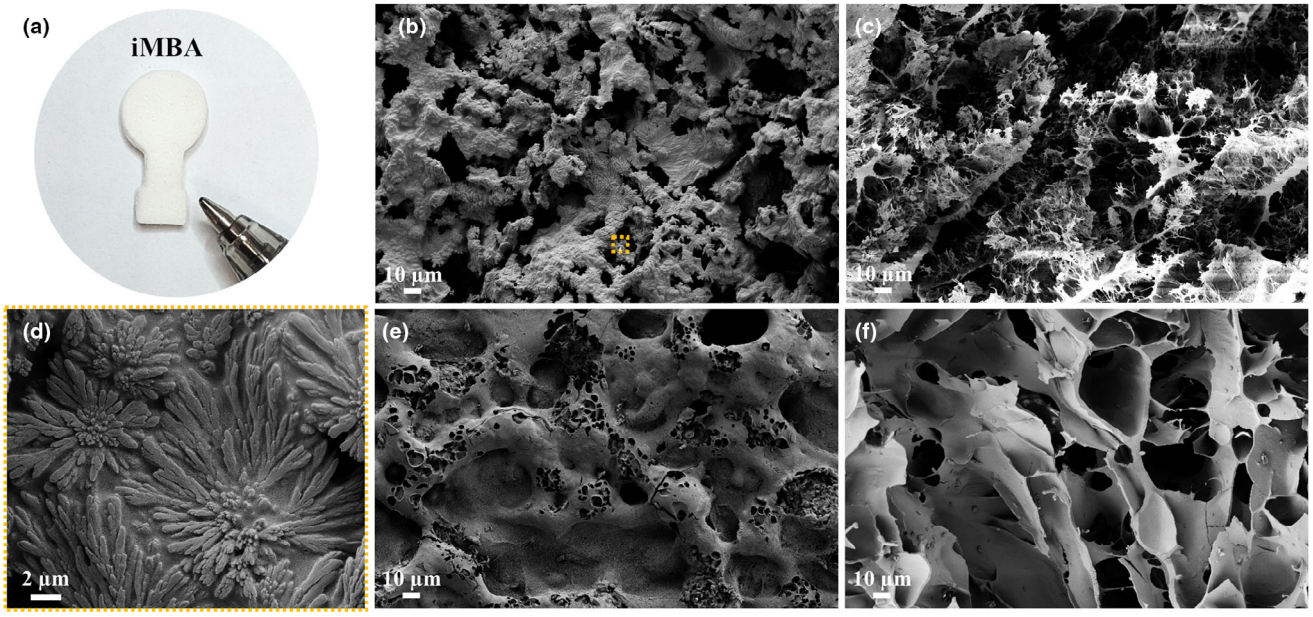

Figure 1. Digital photograph of a) in situ mineralized biomass-derived aerogel (iMBA) prepared using a stereolithography (SLA) 3D printed mold of dimensions: Diameter 10 mm and thickness 3 mm and SEM image of b–d) iMBA (b: top view and its high magnification (d), c: cross-sectional view), and e, f) BA (e: top view, f: cross-sectional view).

diffraction (XRD) results (**Figure 2a**). The diffraction pattern of BA in Figure 2a indicates that alginate/pullulan semi-IPN has a semi-crystalline nature with two distinct peaks at 2θ of 22.5° and 34.5°, as observed previously.[25] Additionally, the spectra showed two amorphous halos with maxima at 2θ values of 15° and 42.5°, attributed to the amorphous pullulan and alginate regions, respectively. On the contrary, the extensive broadening of the characteristic diffraction peaks of pullulan at 2θ of 22.5° and 34.5° in iMBA indicates disruption of the periodic alginate structure by pullulan due to the in situ formation of $CaCO_3$ during the gelation process. The in situ mineralization might have destroyed the close packing of the pullulan molecules necessary to form regular crystallites.[25,26] The XRD pattern also displayed the presence of an amorphous halo arising from the alginate.[27] These results imply that the polysaccharide chains within the iMBA matrices portrayed a more amorphous character. Besides, iMBA possessed sharp diffraction peaks at 2θ values of 20.9°, 24.7°, 27.8°, 32.3°, 43.8°, and 50.1° assigned to the (004), (110), (112), (114), (300), and (118) crystallographic planes of vaterite type $CaCO_3$ (ICSD 15879), respectively.[28,29] This reveals that the microscopic discrete hierarchical flower-like $CaCO_3$ microparticles in situ synthesized within iMBA (Figure 1d) were of pure vaterite phase.

Fourier transform infrared spectroscopy (FTIR) was used to gain further insights into the microstructure of the in situ formed $CaCO_3$ within the structured alginate/pullulan hydrogel (Figure 2b). Compared to BA, the prominent vibration band at 1410 cm^{-1} became wider and shifted in iMBA, owing to the symmetric CO_3 stretching vibration in iMBA caused by the in situ formed carbonate species, in addition to the symmetric O–C–O stretching vibration caused by the glycosidic linkages in polysaccharides.[30] Furthermore, a new peak emerged at 872 cm^{-1} for iMBA associated with the characteristic CO_3 band of the vaterite phase.[29,31] Besides, it was interesting to observe that no absorption bands were recorded at 854 and 848 cm^{-1}, corresponding to aragonite and calcite, respectively, indicating the in situ formed $CaCO_3$ particles were purely of vaterite phase.

High-resolution XPS measurements further confirmed the difference in the chemical composition of iMBA and BA, as shown in Figure 2c. The survey spectra displayed C 1s, O 1s, and Ca 2p in both BA and iMBA. However, the Ca/O atomic ratio of BA and iMBA obtained from XPS was 0.07 and 0.24, respectively. These results confirm the presence of more calcium in the iMBA due to the in situ synthesis of $CaCO_3$ in addition to the Ca^{2+} ions that are cross-linking with adjacent alginate chains to form the ¨egg-box¨ structure in semi-IPN hydrogel via Ca–OOR interactions (Table S2, Supporting Information).[32] The deconvolution of the C 1s spectra of iMBA (Figure S3a, Supporting Information) further demonstrated the existence of CO_3 species from vaterite, with the most intense peak a 289.9 eV.[33] The spectrum also displayed the presence of non-oxide C such as C=C (sp^2, 284.7 eV), C–C (sp^3, 285.2 eV), C–O bonds (286.8 eV), carbonyl C (C=O, 288.3 eV) and carboxylate C (O–C=O, 291 eV), which are functional groups typically present in alginate and pullulan polysaccharides.[34] Moreover, the reasonably strong satellite features corresponding to the $CaCO_3$ microparticles were also observed. The deconvolution of O 1s spectra of iMBA (Figure S3b, Supporting Information) further confirmed the existence of in situ formed $CaCO_3$ microparticles in iMBA with the peak position attributed to the CO_3 in vaterite (*ca.* 531.7 eV) in addition to the C-O (*ca.* 532.8 eV), C=O (*ca.* 532 eV), O–C=O (*ca.* 532 eV) and physisorbed/chemisorbed water (C–OH. . .H) at the sample surface (*ca.* 533.2 eV). The deconvolution of the high-resolution Ca 2p spectrum (Figure 2d) of iMBA showed the characteristic spin-orbit split doublets at *ca.* 347 and 351.2 eV, the $2p_{3/2}$ and $2p_{1/2}$ states, respectively, which could each be further split into two peaks. The first $2p_{3/2}$ component with a binding energy of *ca.* 347.6 eV predominantly indicated the presence of $CaCO_3$. The second $2p_{3/2}$ component at 347.8 eV was attributed to the Ca–OOR interactions in the egg-box

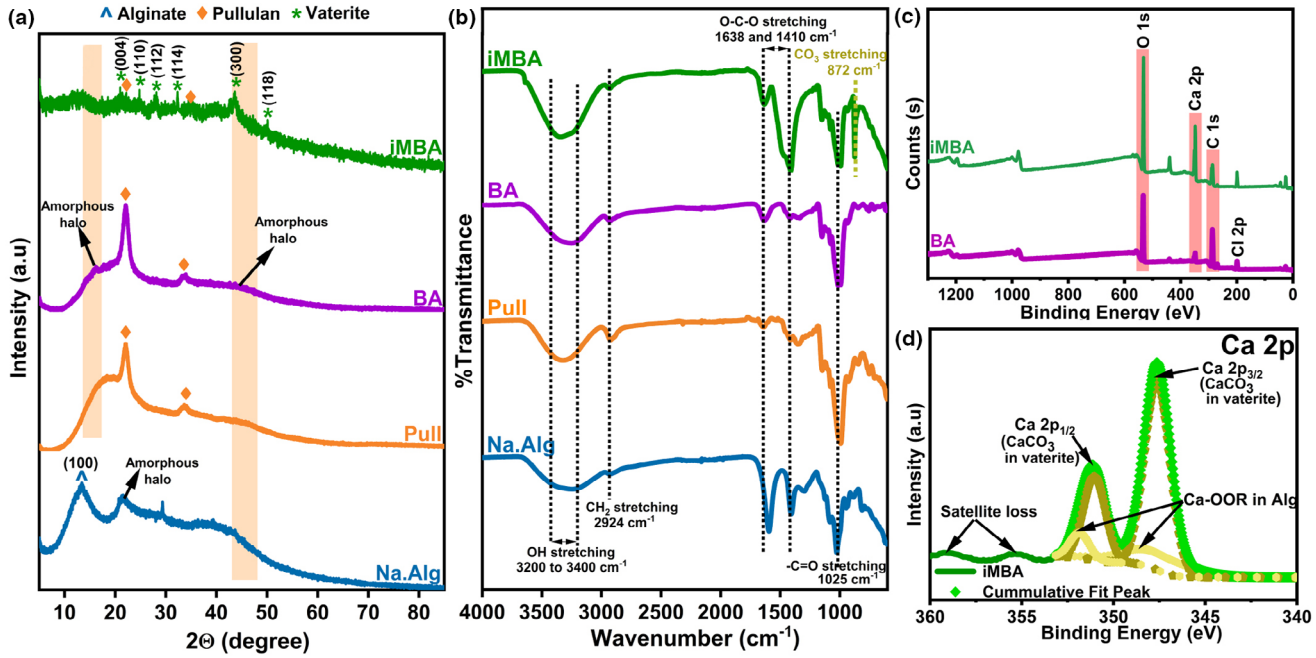

Figure 2. Physico-chemical characterization of in situ mineralized biomass-derived aerogel (iMBA) and BA. a) X-ray powder diffraction (XRD) pattern and b) Fourier transform infrared spectroscopy (FTIR) spectra of sodium alginate (Na.Alg), Pullulan (Pull), BA, and iMBA; c) Full X-ray photoelectron spectroscopy (XPS) spectra of BA and iMBA and d) High-resolution Ca 2p XPS spectra of iMBA.

model formed during the ionotropic gelation of the poly α-l-mannuronate present in the polysaccharide alginate with Ca^{2+} ions. These results indicate that in situ formed $CaCO_3$ microparticles were intimately dispersed within the semi-IPN network of iMBA along with the calcium from Ca-OOR of alginate, while BA only contained the calcium ions used for the formation of egg-box structure. All these observations from SEM, XRD, FTIR, and XPS indicate that metastable, well-dispersed flower-like vaterite microstructures were formed during the fabrication of shapeable free-standing alginate/pullulan semi-IPN hydrogels using the 3DMASC-iMAG strategy when the appropriate concentrations of KOH and $CaCl_2$ cross-linker were used.

2.3. Enhanced Porosity of 3D Carbon Aerogels Prepared with iMAG

The lyophilized iMBA were pyrolyzed at 900°C under an inert atmosphere followed by a mild acid washing step in 1 M HCl to demineralize the resulting carbon structures. The one-step activation-graphitization of the iMBA resulted in a carbon aerogel (iMBCA) through depolymerization and aromatization, whilst the in situ formed $CaCO_3$ served as a pore generating agent by decomposing into CaO and CO_2 and acting as a catalyst for graphitization.[35] After demineralization by etching, it was impressive to see that the yielded iMBCA-E (**Figure 3**a,b) with a density as low as ~0.14 g/cm^3 obtained after a carbonization-induced mass loss of ~52% could retain the structural integrity and remarkable mechanical stability, which allowed them to support approximately 15 000 times its own weight without any visible damage (Figure S4 and Movie S2, Supporting Information**).**

For comparison, aerogels without mineralization (BA) were subjected to the same process for conversion into BCA-E. As seen from the SEM images, compared to pure mesopores for BCA-E (Figure 3c,d), iMBCA-E (Figure 3e,f), a highly interconnected, honeycomb-like porous 3D network structure with macropores, mesopores, and dense micropores. The high-resolution SEM images of the walls of the macropores (Figure 3f) confirmed that iMBCA-E had a rough surface with dense micropores of irregular shape. The high-resolution TEM image (Figure 3g) of iMBCA-E revealed the co-existence of amorphous and graphitic structured carbon in the sample. The preparation of such lightweight free-standing electrodes with a hierarchical and well-interconnected porous structure with amorphous and graphitic domains should provide an excellent pathway with improved wettability for the rapid transport of electrons to the interior surface and shorten the ion diffusion distance, potentially leading to enhanced electrode/electrolyte interface.[9,36]

The XRD of iMBCA before the mild acid etch and water wash (**Figure 4**a) revealed that the in situ-formed $CaCO_3$ evolved to CaO particles, suggesting its decomposition into CaO and $Ca(OH)_2$ during high-temperature pyrolysis via a series of reactions (Equations 3 and 4).[37–39] In addition, the gaseous CO_2 evolved during the decomposition of the in situ-formed $CaCO_3$ porogen could further induce porosity in the carbon through the CO_2 inner-activation effect.

$$CaCO_3 \rightarrow CO_{2(g)} + CaO \quad (3)$$

$$CaO + H_2O\ (\text{humidity}) \rightarrow Ca(OH)_2 \quad (4)$$

The resultant CaO and other inorganic impurities encapsulated within the carbonized semi-IPN network were removed during the mild acid etching and water-washing step, resulting in iMBCA-E. Besides, the acid washing also assisted in opening up the

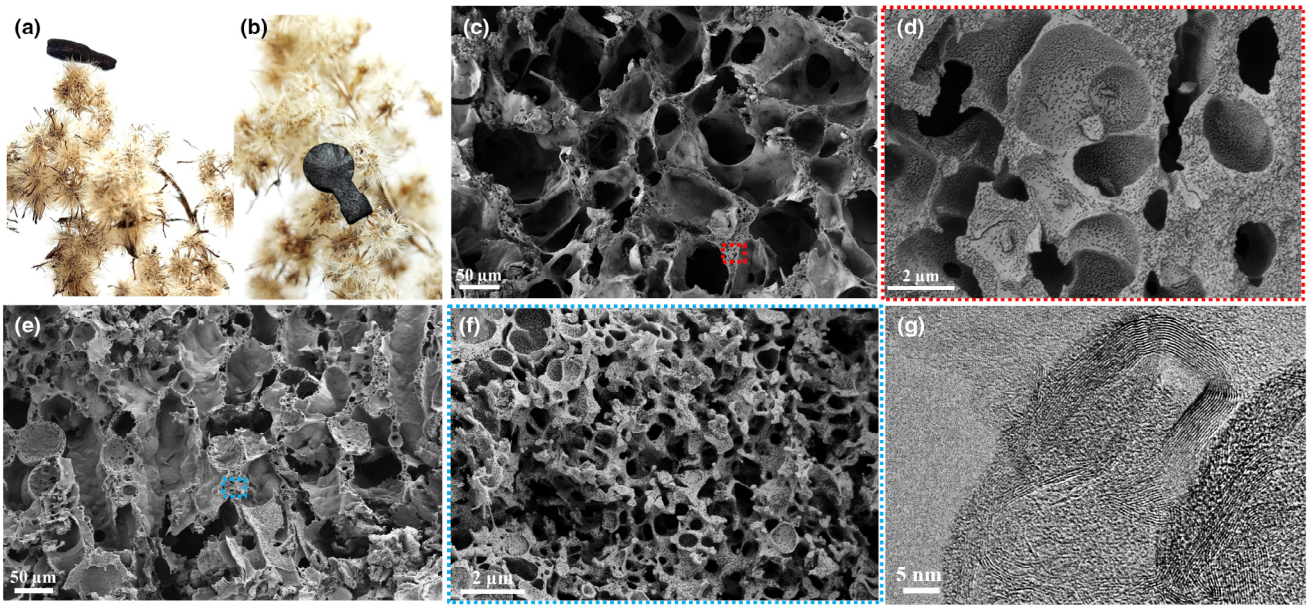

Figure 3. a, b) Digital photographs of lightweight iMBCA-E prepared using SLA 3D printed master mold of diameter 10 mm and thickness 3 mm (a: side view and b: top view) supported on dandelion flower, SEM image of c, d) BCA-E (c: low-mag; d: high-mag), e, f) iMBCA-E (e: low-mag; f: high-mag), and g) High-resolution TEM image of iMBCA-E.

micropores formed during the etching of the carbon framework by the CO_2 gases.[40] The successful removal of CaO from iMBCA was revealed from the XRD pattern of iMBCA-E, as shown in Figure 4a. Compared to iMBCA, post-acid etching followed by water washing resulted in high-purity carbon materials without calcium moieties. The pyrolysis of BA prepared without mineralization resulted in BCA-E with two sharp and narrow diffraction peaks around 2θ of 22.6° and 25.8°, corresponding to the (002) reflection of the disordered (labeled as c_d in Figure 4a) and graphitic carbon (labeled as c_g in Figure 4a), respectively, and a broad peak at 2θ of 43.6°, corresponding to the (100) reflection of the graphite structure.[41] The peak shift to the left compared to standard graphite (2θ of 26.6°) indicates that interlamellar spacings of the pyrolytic carbon became broader than standard graphite. In comparison, for iMBCA-E (Figure 4a), the (002) peak around 2θ of 25.8° completely disappeared, indicating a highly disordered graphitic structure. A more detailed investigation at variable carbonization temperature was performed. As seen from Figure 4b, at a lower carbonization temperature of 700 °C, a sharp and narrow diffraction peak around 2θ of 22.6° and a small broad peak at 2θ of 43.6° were observed, corresponding to the presence of disordered and graphitic carbon.[41] The presence of a sharp diffraction peak at 700 °C indicates that the carbon derived from biomass materials is more amorphous and is similar to earlier reports on alginate-derived carbon materials.[12,42] With the increase in carbonization temperature, the intensity of the disordered carbon peak at 2θ of 22.6° was gradually reduced, and at temperatures of 900 °C and above, the peak became broader, and a distinct peak corresponding to graphitic carbon at 2θ of 23.9° starts to appear. Moreover, the presence of a more pronounced peak at 2θ of 43.6° for temperatures above 900 °C indicates that the use of higher carbonization temperature above 900 °C is required to produce a more graphitic carbon. However, the presence of a broad peak at 2θ of 22.6° along with a slightly pronounced peak at 2θ of 43.6° for iMBCA-E samples carbonized at 900 °C indicates that a sufficient amount of graphitization has occurred, resulting in the successive transformation of the alginate/pullulan semi-IPN precursor material into potentially conductive pyrolytic carbon with co-existence of regions with amorphous and graphitic structures.[43] Thus, iMBCA-E pyrolyzed at 900 °C possesses some oriented and interlinked porosities in addition to the disordered stacking of micro graphites and is in agreement with the TEM results. The appropriate co-existence of amorphous and graphitic carbon in iMBCA-E is believed to improve its wettability, which is essential for applications requiring enhanced mass transport.[40,41,44]

The microstructural changes due to the one-step activation-graphitization of iMBA with confined $CaCO_3$ had a significant effect on the surface area and pore size distribution of iMBCA-E. The N_2 adsorption/desorption isotherm curves (Figure 4c) revealed that BCA-E mostly displayed mesopores. In contrast, for iMBCA-E, a significant adsorption volume occurred over the entire pressure range, indicating the co-existence of micro- and mesopores. Compared to BCA-E (S_{BET}: 101.94 $m^2\ g^{-1}$ and pore volume: 0.07 cm^3/g), iMBCA-E exhibited a higher Brunauer–Emmett–Teller (BET) surface area (S_{BET}: 327.4 $m^2\ g^{-1}$) along with a larger pore volume (0.28 cm^3/g) and relatively wider pore size distribution (Figure 4d) with more prominent pores around 1 nm (Table S1, Supporting Information). The transformation of polysaccharides into a condensed aromatic system around the CaO and the simultaneous activation of the carbon materials by the CO_2 through the inner-activation effect favored the formation of hierarchical pore structures with micro- and mesoporosity in iMBCA-E. This indicates that $CaCO_3$ formed during the hydrogel preparation process was not agglomerated but relatively homogeneously distributed, translating into enhanced microporosity. In addition, the higher degree of disordering as suggested by the Raman spectra (Figure 4e) with an I_D/I_G (Intensity ratio of the D-band to the G-band) of 0.99 for iMBCA-

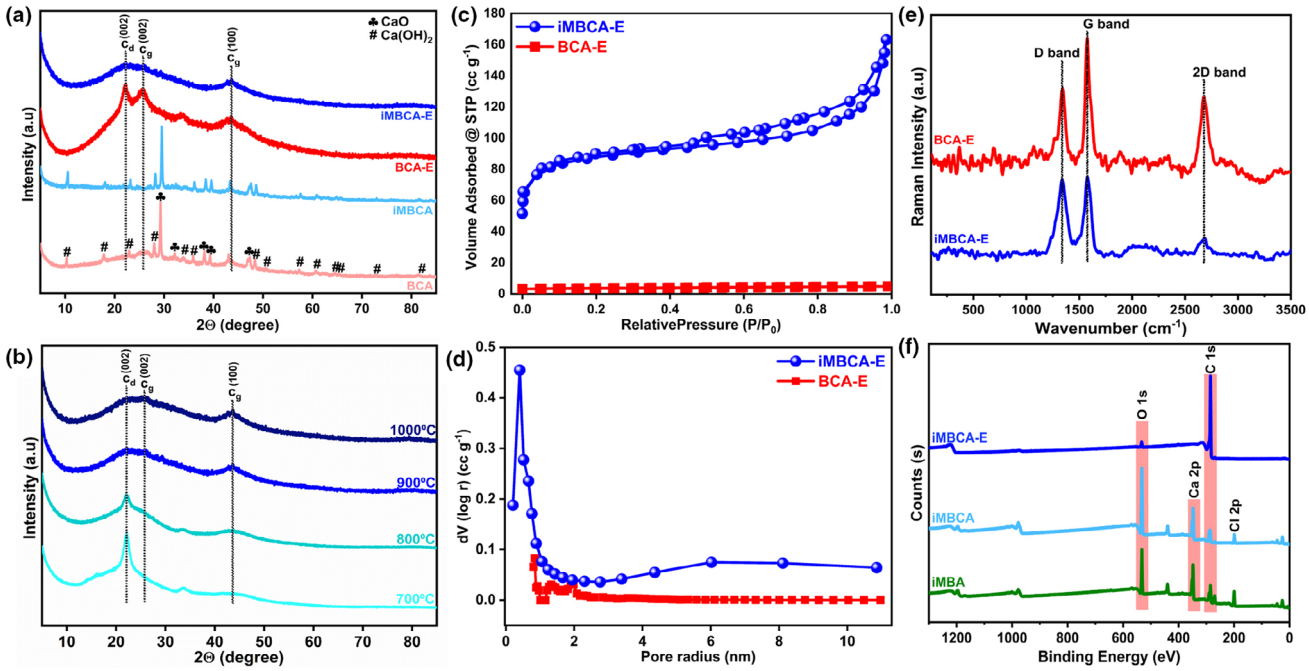

Figure 4. X-ray powder diffraction (XRD) pattern of a) BCA-E and iMBCA-E pyrolyzed at 900 °C and b) of iMBCA-E obtained after pyrolysis at different temperatures, c) Nitrogen adsorption–desorption isotherms and d) its corresponding pore size distribution curves, e) Raman spectra of BCA-E and iMBCA-E obtained after pyrolysis at 900°C, and f) XPS full survey spectra of iMBA, iMBCA, and iMBCA-E. E represents that acid etching and water washing were performed for these samples.

E and 0.59 for BCA-E, further confirms the development of microporosity in iMBCA-E because the decomposition of in situ $CaCO_3$ resulted in the formation of defective structures in the carbon structure.[40] Besides, Raman spectra revealed the presence of a broader 2D peak, the characteristic graphene peak, in iMBCA-E compared with the BCA-E (sharp and visible peak), indicating a layered structure of carbon with a few layers of graphene. A slightly higher increase in the ratio of 2D and G band intensities (i.e., I_{2D}/I_G) of iMBCA-E (i.e., 0.72) over BCA-E (i.e., 0.52) further suggests that iMBCA-E has a highly porous graphitic structure with increased content of structural disorder and defective carbon structures compared to BCA-E.[45] This is attributed to the role played by the in situ-formed $CaCO_3$ particles as pore-generating agents during one-step activation-graphitization.

The full survey XPS spectra obtained following one-step activation-graphitization before (iMBCA) and after mild acid etching followed by water washing (iMBCA-E) (Figure 4f) showed distinct differences compared to the precursor iMBA (Figure 2c). The sharp C and O peaks at binding energies 285 and 533 eV were observed in all the samples, while Ca peaks (348 eV) only were present in iMBA and iMBCA. The corresponding concentrations of C, O, and Ca elements are listed in Table S2, Supporting Information. In addition, the presence of Cl 2p (Figure 4e) with a peak at a binding energy of 199 eV indicates its existence in iMBCA. Most likely, Cl is embedded into the aerogel matrix during ionotropic gelation of alginate with $CaCl_2$. In comparison, all the characteristic Ca 2p, and residual Cl 2p peaks were absent in the XPS spectra of iMBCA-E obtained after mild HCl etching followed by water wash, most likely due to the etching of CaO and removal of other impurities. As expected, the analysis of the C 1s peak (Figure S3c, Supporting Information) indicates that the pronounced CO_3 species observed in iMBA (Figure S3a, Supporting Information) (289.9 eV) disappeared in iMBCA-E, further confirming the successful decomposition of $CaCO_3$ to CaO followed by its removal during acid washing. The pronounced increase in the intensity of the C=C peak in iMBCA-E is mainly due to the π–π interaction of the robust hierarchical 3D interconnected graphitic frameworks formed during one-step activation-graphitization. Moreover, the iMBCA-E had a more substantial sp^3 C–C peak, indicating more structural defects caused by the in situ synthesized $CaCO_3$ microparticles during activation-graphitization, which is consistent with the Raman results.[34] Simultaneously, the O 1s spectra (Figure S3d, Supporting Information) showed different oxygen contributions, which are usually associated with C–O (532.8 eV), C=O (533.2 eV), O–C=O (533.1 eV), physisorbed/chemisorbed water (C–OH. . .H) at the sample surface (533.2 eV) and the defect sites (531.5 eV) and e + species (530.4 eV) with low oxygen coordination in the sample with small particle sizes.

Thus, the iMAG strategy with in situ mineralization of alginate-pullulan semi-IPN with $CaCO_3$ followed by one-step activation-graphitization resulted in a free-standing carbon aerogel with a dense carbon network, hierarchical porous structure (high (ultra-) micro and mesopores) with well-interconnected channels and numerous defects as shown from the SEM, BET, Raman, and XPS, potentially facilitating the interfacial electron transfer and ion diffusion kinetics.[40,44]

2.4. Enhanced Capacitive Energy Storage with in-Situ Mineralized Carbon Aerogels

In light of these above-observed unique features, the as-prepared alginate/pullulan biomass-derived free-standing iMBCA-E should be highly promising high-performance electrode materials for electrochemical

applications such as in supercapacitor devices. As a proof of concept, we evaluated iMBCA-E and BCA-E as binder-free supercapacitor electrodes. To assess their electrochemical performance, cyclic voltammetry (CV) and galvanostatic charge–discharge (GCD) experiments were performed in an electrochemical cell with a three-electrode configuration using 2 M KCl aqueous solution as the electrolyte (**Figure 5**). Compared to BCA-E (non-mineralized route in Scheme 1), iMBCA-E electrode materials prepared with the iMAG approach with different KOH concentrations (0.5 and 1 M) (mineralized route in Scheme 1) displayed a rectangular-shaped CV (Figure 5a), demonstrating an electrical double layer type capacitive behavior.[46,47] Notably, iMBCA-E prepared using 1 M KOH as the dissolution media exhibited a remarkably larger enclosed area in a CV than with 0.5 M KOH and without any KOH (BCA-E), indicating its ability to deliver much higher energy storage capacity. Similarly, the GCD curves recorded for these electrodes displayed a symmetrical triangular shape (Figure 5b) with the longest discharge times in the range of −0.3 to 0.8 V. The higher capacitance indicates efficient electrical double-layer charge storage due to the presence of ion-buffering reservoirs (macropores), ion-highways for fast ion transport (mesopores), and large electrochemically active sites (ultra-micropores) for ion accumulation within these free-standing 3D porous electrodes.[48,49] The calculated gravimetric capacitance (C_g) of iMBCA-E prepared with 1 M KOH is approximately 144.6 F g^{-1}, which is substantially higher than the one of iMBCA-E prepared with 0.5 M KOH and without KOH (BCA-E) (~45 and ~0.01 F g^{-1}, respectively) at the same current density of 0.5 mA cm^{-2}. The well-defined hierarchical porous structure with a large accessible surface area, a high density of micro- and mesoporous channels, and especially ultra-microporosity with pores having widths below 1 nm induced during one-step activation-graphitization boosted the capacitive electrochemical performance of iMBCA-E[50] with a factor > 10 000. Furthermore, the concentration of KOH played a significant role in enhancing the electrochemical performance, as it was responsible for the amount of $CaCO_3$ confined within the semi-IPN network during hydrogel synthesis. The subsequent enhanced pore generation and carbon activation allowed to achieve this specific pore structure, providing electrolyte ion buffering reservoirs and rapid ion diffusion channels contributing remarkably to the electrochemical capacitance. It should be noted, that further increase in the KOH concentration beyond 1 M failed to gelate upon cross-linking.

Figure 5c presents the CV profile of iMBCA-E electrodes prepared at different pyrolysis temperatures in a voltage window of −0.3 to 0.8 V. With the increase in temperature, the area formed by the CV curve of the iMBCA-E electrodes gradually increased up to 900 °C. Below 900 °C, iMBCA-E exhibited a relatively low specific capacitance (32.4 and 61.4 F g^{-1} for 700 and 800 °C, respectively, Figure 5d) due to only partial carbonization. iMBCA-E electrodes pyrolyzed at 900 °C exhibited the largest enclosed area under CV and longest discharge time (Figure 5d), indicating the highest energy storage capability. The large capacitance of 144.6 F g^{-1} delivered by iMBCA-E prepared at 900 °C could be attributed to the formation of more graphitic and conductive carbon, offering a large ion-accessible surface area for efficient charge storage.[44] However, increasing the carbonization temperature beyond 900 °C decreased the specific capacitance (133.7 F g^{-1}), which might

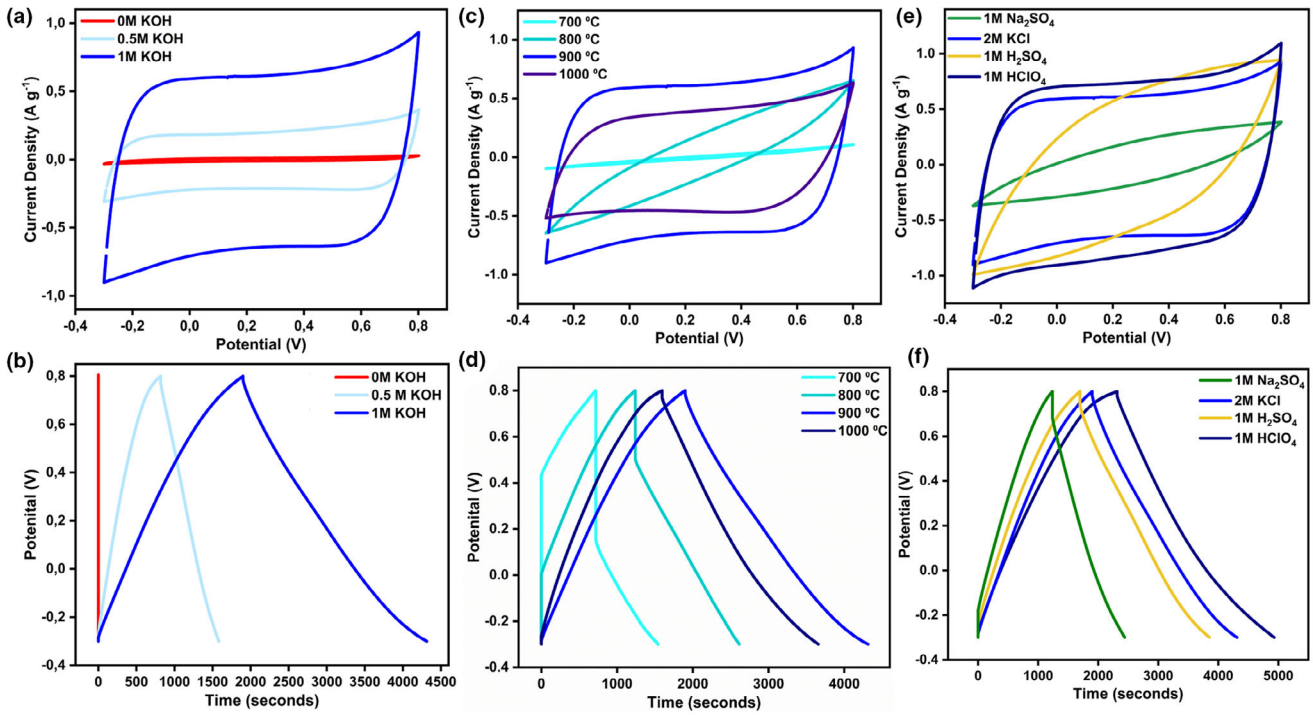

Figure 5. Comparison of a) CV and b) galvanostatic charge–discharge (GCD) of the iMBCA-E prepared with a KOH concentration of 0.5 M, 1 M, and without KOH (BCA-E) pyrolyzed at 900 °C in a three-electrode cell configuration employing 2 M KCl aqueous electrolyte; c) CV and d) GCD profiles of iMBCA-E electrodes prepared at different pyrolysis temperatures measured in 2M KCl; e) CV and f) GCD of iMBCA-E pyrolyzed at 900 °C in different electrolytes. All electrodes used for the electrochemical characterization were fabricated with a mold with a diameter of 10 mm and a depth of 3 mm. All CVs and GCDs were performed at a scan rate of 5 mV s^{-1} and a current density of 0.5 mA cm^{-2}, respectively.

be attributed to the collapse of the porous carbon network during high-temperature carbonization.[51] Thus, based on the structural, morphological, and electrochemical analysis, a temperature of 900 °C was the optimum for obtaining an efficient free-standing 3D hierarchical porous carbon aerogel-based supercapacitor electrode with an interconnected porous graphitic carbon structure for improved mass transport and rapid electron transfer. Preliminary CV experiments at 5 mV s^{-1} within different potential windows showed that iMBCA-E electrodes exhibited exemplary capacitive behavior with nearly rectangular CV curves and without any apparent polarization even at a potential window of −0.5 to 0.8 V in 2 M KCl, further supporting the excellent capacitance characteristics (Figure S6a,b, Supporting Information). However, rectangular-shaped CV curves along with symmetrical GCD curves were only observed within voltage windows −0.3 to 0.8 V. Hence, this voltage window was selected for performing further detailed electrochemical characterization.

The capacitance behavior and efficiency of iMBCA-E in different media were analyzed by performing electrochemical experiments in four aqueous electrolytes (2 M KCl, 1 M Na_2SO_4, 1 M H_2SO_4, and 1 M $HClO_4$) in a voltage window of −0.3 to 0.8 V. As seen in Figure 5e, iMBCA-E displayed rectangular-shaped CVs with a rapid current response on voltage reversal at the two end potentials in 1 M $HClO_4$ and 2 M KCl, confirming an excellent capacitive behavior in these electrolytes. However, the free-standing iMBCA-E electrodes displayed poor capacitive behavior with a largely deformed CV curve in 1 M Na_2SO_4 and 1 M H_2SO_4 (typical acidic) aqueous electrolytes. The specific capacitance values derived from GCD curves in different electrolytes, as shown in Figure 5f, were 72.2, 129.3, 144.6, and 188.2 F g^{-1} at 5 mV s^{-1} for 1 M Na_2SO_4, 1 M H_2SO_4, 2 M KCl, and 1 M $HClO_4$, respectively. The significant difference in the CV shapes and specific capacitance values in different electrolytes are attributed to the difference in hydration sphere radius of cation/anion, their conductivity and ionic mobility. The hydrated cation radius of the studied electrolytes was in the order of H^+/H_3O^+ (2.8 Å) < K^+ (3.31 Å) < Na^+ (3.58 Å), while the radius of the anions was in the order of Cl^- (3.32 Å) < ClO_4^- (3.38 Å) < SO_4^{2-} (3.79 Å).[52] Even though Cl^- and ClO_4^- anions have almost the same hydration sphere radius, the smaller hydration sphere radius of H^+ cations, along with the higher conductivity of 350.1 S cm^2 mol^{-1} as compared to K^+ ions (73.5 S cm^2 mol^{-1}), enhanced the ionic mobility and interaction with the electrode material, resulting in higher current response and specific capacitance for $HclO_4$. On the contrary, the larger radius of the hydration sphere of SO_4^{2-} anions, along with low conductivity and ionic mobility, leads to a decreased diffusion of ions in the pores, resulting in poor capacitive behavior in both H_2SO_4 and Na_2SO_4 electrolytes.[53,54] These results indicate that the iMBCA-E electrode exhibited enhanced electrochemical performance in 1 M $HclO_4$ aqueous electrolyte with cation intercalation as the dominant charge storage mechanism.

2.5. Exploring 3D Electrode Design Flexibility with 3DMASC-iMAG

In general, 3D printing allows for prototyping with high freedom of design, achieving molds with excellent structural resolution (25 μm), and almost arbitrary overall dimensions. Here, 3D printing-driven mold-assisted solution casting (3DMASC) was introduced as an innovative approach for fabricating 3D hydrogel structures in a highly reproducible manner. To further demonstrate the versatility of the iMAG fabrication process using 3DMASC, iMBH, iMBA, and iMBCA-E were fabricated with varying diameters (D) ranging from 6 to 12 mm and a fixed thickness (T) of 3 mm as displayed in **Figure 6a**. The CV and GCD of these tailored iMBCA-E electrodes are shown in Figure 6b, c, respectively. As expected, higher electrochemical current responses and larger integrated areas under the CV curves are observed with an increase in the mold diameter from 6 to 12 mm (Figure S6c, Supporting Information). However, increasing the diameter of an electrode also increases the active mass loading, which often results in a significant drop in specific capacitance due to the increase of ion transport distance and deterioration of ion accessibility.[55,56] The C_g calculated from the GCD curves (Figure 6c) for iMBCA-E electrodes prepared from molds with diameters of 6 and 8 mm was maintained at ~322 F g^{-1}. For further increase of the mold diameter to 10 and 12 mm, the C_g decreased to ~199 F g^{-1}, which is ~62.8% of the C_g of iMBCA-E electrodes prepared with D = 6 and D = 8 mm. In contrast to the increase in current response due to more electroactive surface area, the C_g decreased for electrodes prepared with mold diameters greater than 8 mm. As the diameter of the electrode increases, the internal resistance of the electrode increases, thereby resulting in a potential drop at the edge of the electrodes. Consequently, higher diameter electrode materials only contribute partially to charge storage. Therefore, for achieving higher capacitances, it might be advantageous to have several iMBCA-E electrodes prepared with smaller mold diameters connected in series rather than further increasing the dimensions of iMBCA-E electrodes. The designs in this study are chosen to illustrate the design flexibility of the method. However, a detailed investigation should be performed to conclude the relationship between dimensions, shape, and electrochemical performance.

2.6. Electrochemical Performance and Cyclic Stability for Optimized 3D Electrode

A comprehensive evaluation of the electrochemical performance of iMBCA-E prepared using a mold with D = 8 mm was carried out through CV and GCD at different scan rates (**Figure 7a**) and current densities (Figure 7b), respectively, in a three-electrode set-up. The quasi-rectangular shape was well preserved at scan rates ranging from 2 to 30 mV s^{-1}, indicating that the electrical double layer with highly reversible and kinetically facile charge–discharge responses are still the predominant capacitive characteristic. However, the rectangular shape is distorted with increasing to higher scan rates. There, the H^+ ions did not have sufficient time to diffuse into the pores of the hierarchical porous 3D free-standing iMBCA-E electrode, thereby hindering the accessibility of electrolyte ions to the inner pore sites.[52] Impressively, when the current densities are further increased from 0.5 to 10 mA cm^{-2}, charge/discharge plots Figure 7b) showed typical electrochemical double-layer capacitance characteristics with a triangular shape, indicating the excellent charge diffusion at the iMBCA-E electrode interface during adsorption/desorption. At various current densities of 0.5, 1, 2, 3, 5, and 10 mA cm^{-2}, the C_g of iMBCA-E in 1 M $HClO_4$ remained at 322.1, 186.8, 161.4, 147.8, 128.3, 96.2 F g^{-1}, respectively (Figure 7c). The decrease in capacitance with an increase in the current density was on account of the insufficient surface contact and hindrance of ions diffusing into the internal pores of the hierarchical porous free-standing iMBCA-E electrode.[57] However, to the best of the author's knowledge, the capacitance of the as-fabricated free-standing iMBCA-E

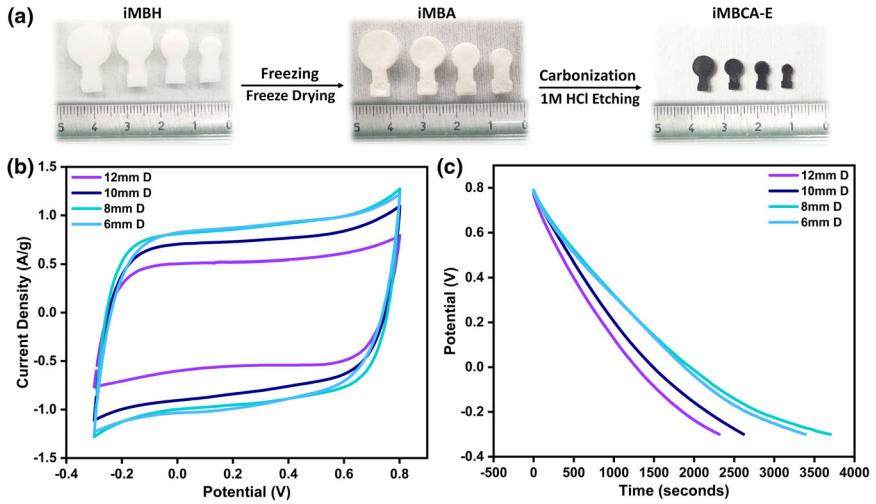

Figure 6. a) Digital photographs of iMBH, iMBA, and iMBCA-E prepared using SLA 3D printed master molds of different diameters ranging from 6 to 12 mm and a depth of 3 mm and b) CV and c) galvanostatic charge–discharge (GCD) of iMBCA-E electrodes fabricated using different master molds at a scan rate of 5 mV s^{-1} and a current density of 0.5 mA cm^{-2}, respectively.

electrodes is higher than other free-standing (Table 1) and powdered biomass-derived EDLC-based carbon electrodes (Table S3, Supporting Information).

Figure 7d illustrates the long-term electrochemical cyclic stability of iMBCA-E fabricated with a 3D printed mold with a diameter of 8 mm and thickness of 3 mm for GCD at a current density of 5 mA cm^{-2} in a three-electrode set-up. The excellent electrochemical stability of hierarchical porous iMBCA-E free-standing electrodes is further demonstrated in Figure 7e and Figure S6d, Supporting Information. The results show that the electrode displayed a rectangular-shaped CV (Figure 7e) without any noticeable distortion and nearly symmetric charge–discharge curves (Figure S6d, Supporting Information) even after long periods of continuous charge–discharge. More surprisingly, the iMBCA-E electrode presented an increasing capacitance trend with specific capacitance retention of 104% after 1000 consecutive charging/discharging cycles. This outstanding capacitance retention could be ascribed to the porous nature of the as-prepared free-standing iMBCA-E electrodes with hierarchical pores. In the initial cycles, only large pores and mesopores might be infiltrated by electrolytes. Nevertheless, during the repeated cycling process, the hydrated H^+ ions can gradually penetrate the micropores due to good inter-pore

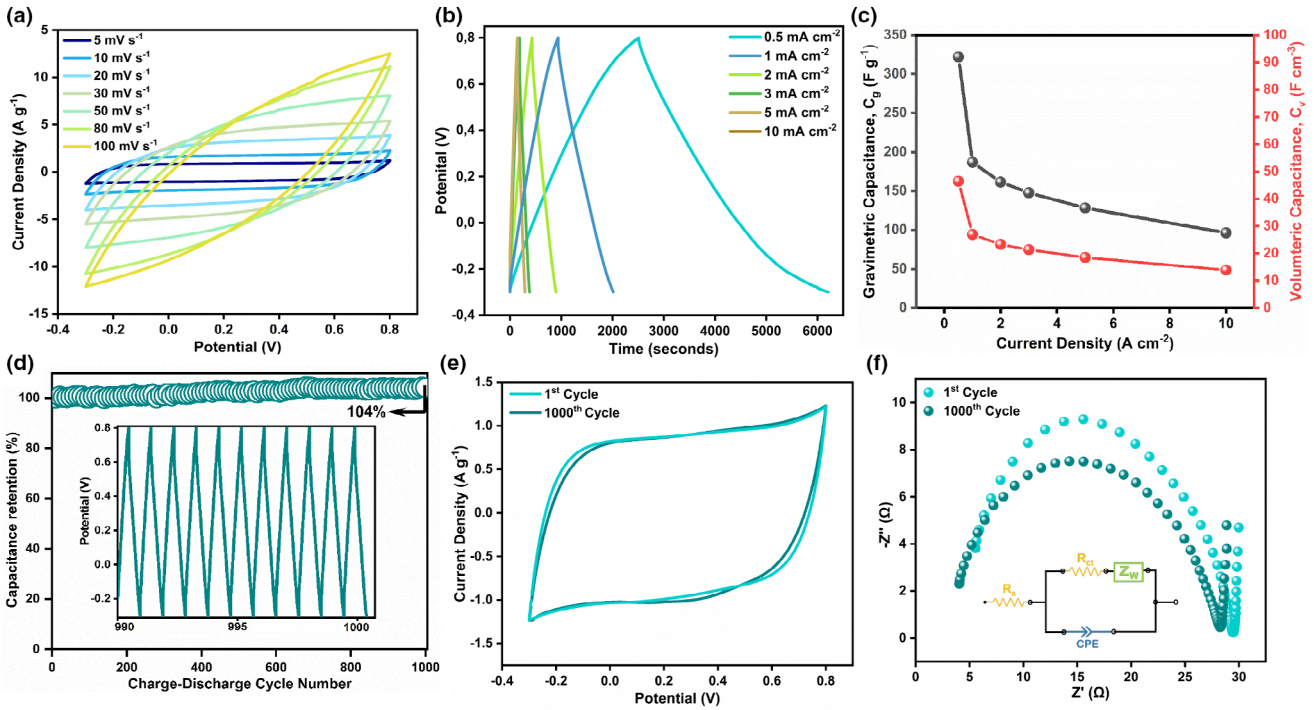

Figure 7. The electrochemical performance of iMBCA-E electrodes (Diameter-8 mm and Thickness-3 mm) in a three-electrode set-up with 1 M $HClO_4$ as electrolyte. a) CV profiles at different scan rates (5–100 mV s^{-1}); b) galvanostatic charge–discharge (GCD) curves at different current densities (0.5–10 mA cm^{-2}); c) Gravimetric and volumetric capacitance of iMBCA-E as a function of current density (0.5–10 mA cm^{-2}); d) Cycling performance at 5 mA cm^{-2} in the potential window of −0.3 to 0.8 V; e) CV profiles and f) Nyquist plot obtained from the electrochemical impedance spectroscopy (EIS) measurements with the frequency range of 0.1 Hz–100 kHz after 1st and 1000th charge/discharge cycles. The inset in panel d) displays the GCD curves of the last 11 charge/discharge cycles.

Table 1. Comparison of free-standing biomass-derived EDLC based carbon aerogels as electrodes for supercapacitors.

Sample	Biomass	Pyrolysis Temp (°C)	Post activation	Potential Window (V)	Conditions	Capacitance F/g	References
NCCF	Bacterial Cellulose	800	HNO_3/H_2SO_4 (v/v = 1/3)	−1 to 0	0.1 A/g, three-electrode, 6 M KOH	250	14
PBC-N	Bacterial Cellulose	900	Urea doping	0 to 1	1 A/g, two-electrode, 6 M KOH	129	15
			Hydrothermal, 180 °C				
A-p-BC-N	Bacterial Cellulose	600	CO_2 at 800 °C	0 to 1	1 A/g, two electrode, 2 M H_2SO_4	195.4	18
PCF	Chitosan	800	-	−0.8 to 0	0.5 A/g, two electrode, 3 M KOH	246.5	19
CF	Natural Cotton	800	-	0 to 1	1 A/g, three-electrode, 6 M KOH	122	20
aCF			2 M KOH			283	
SLC	Lignin	900	NaOH	−1 to 0	0.1 A/g, three-electrode, 6 M KOH	208.4	21
MCM	Sucrose	650	-	0 to 2.5	10 mV/s, two-electrode, EMITFSI	75	22
iMBCA-E	Alginate/pullulan	900	-	−0.3 to 0.8	0.5 mA cm^{-2}, three-electrode, 1 M $HClO_4$	322	This work
				0 to 1.2	0.5 mA cm^{-2}, two-electrode, 1 M $HClO_4$	376	

connection and participate in establishing electric double layers.[58] On account of the high-level utilization of the pores, after the repetitive charge–discharge process, the iMBCA-E electrode material tends to reach a stable capacitance value, thus showcasing outstanding cyclic stability. Furthermore, the equivalent series resistance (ESR) of the electrode calculated from the intersection of the Nyquist plots to the real axis in the high-frequency region (Figure 7f) decreased from ~2.98 to 2.20 Ω after 1000 cycles. This can again be ascribed to the improvement of the electrolyte/electrodes interface caused by the thorough wetting of the pores, allowing for improved ion transport. These results further confirm the high degree of reversibility and excellent cycle stability of 3D iMBCA-E, which are desirable properties for high-quality supercapacitive electrochemical energy storage applications. The superior performance of 3D free-standing iMBCA-E for supercapacitive energy storage can be attributed to the in situ synthesized $CaCO_3$ template, which generated numerous defects and hierarchical porous structure (high micro and mesopores) with well-interconnected channels during one-step high-temperature activation-graphitization, facilitating the interfacial electron transfer and ion diffusion kinetics. Unlike other carbon materials derived from alginate, the use of free-standing iMBCA-E as an electrode for supercapacitor does not require any particular substrates or transfer procedures, further illustrating the advantage of utilizing the iMAG strategy with 3DMASC for precursor preparation.

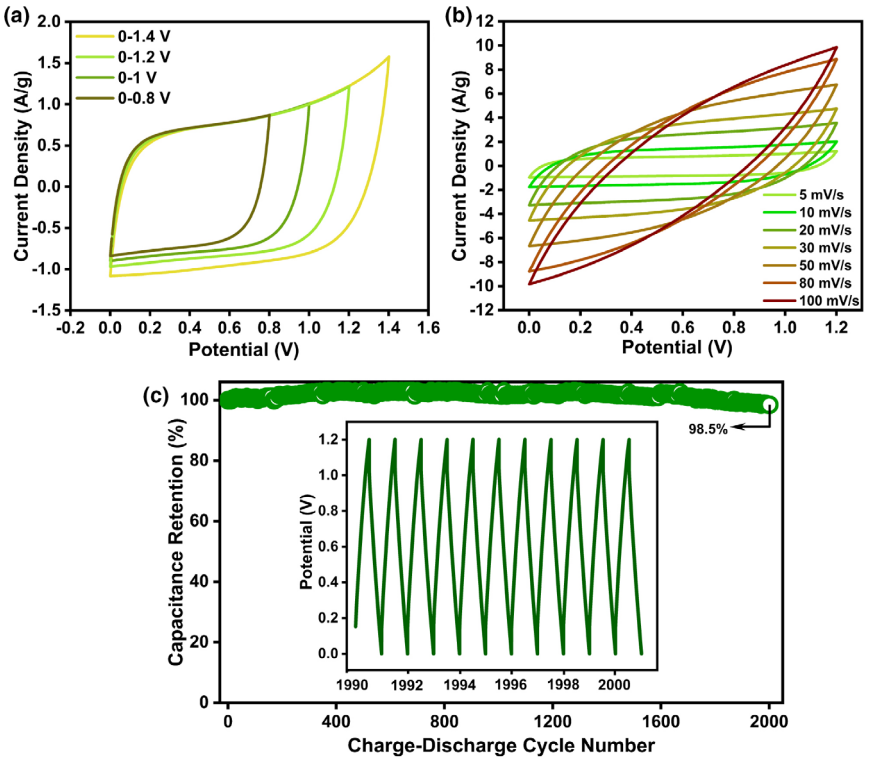

Figure 8. The electrochemical performance of a symmetric supercapacitor (SSC) fabricated using two iMBCA-E electrodes (Diameter-8 mm and Thickness-3 mm) with 1 M $HClO_4$ as electrolyte. a) CV curves under different operating potentials; b) CV curves at various scan rates (5–100 mV s^{-1}) and c) Cycling stability at 3 mA cm^{-2} in the potential window of 0–1.2 V. The inset in panel c) shows the GCD curves of the last 11 charge/discharge cycles.

2.7. Electrochemical Performance of Symmetric Supercapacitor

For a first indication of the practical applicability, the electrochemical properties of free-standing iMBCA-E electrodes were evaluated by assembling a two-electrode symmetric

supercapacitor (SSC) using two identical iMBCA-E electrodes separated by a borosilicate glass microfiber filter (~100 μm thick, GF/D, Whatman) and soaked in 1 M $HClO_4$ aqueous electrolyte. **Figure 8a** depicts the CV curves of the iMBCA-E//iMBCA-E based SSC at different operating voltage windows from 0–0.8 V to 0–1.4 V at a scan rate of 5 mV s^{-1}. The quasi-rectangular shape was well preserved for all the CV curves, indicating that no parasitic reactions occurred and that the SSC device can work for up to 1.4 V. In the potential window of 0–1.2 V, the assembled SSC device retained a relatively rectangular CV shape without apparent distortion even at 50 mV s^{-1} (Figure 8b), suggesting a fast capacitive behavior. However, at higher scan rates, the rectangular shape was distorted owing to the insufficient time for the H^+ ions to diffuse into the pores of the hierarchical porous 3D free-standing iMBCA-E electrode. The calculated specific capacitance of the iMBCA-E-based two-electrode SSC device was 376 F g^{-1} at a current density of 0.5 mA cm^{-2}. Furthermore, the iMBCA-E-based SSC device displayed a high energy density of 26 W h kg^{-1} at a power density of 4000 W kg^{-1}. Moreover, as shown in Figure 8c, the long-term charge–discharge test conducted using the iMBCA-E//iMBCA-E SSC at a constant current of 3 mA cm^{-2} revealed that the iMBCA-E electrode maintained a final specific capacitance retention of about 98.5% after 2000 cycles, which embodies its remarkable cycling stability and high reversibility. The obtained specific capacitance and capacitance retention of iMBCA-E in two-electrode SSC surpasses those reported for other free-standing (Table 1) and powder-based (Table S3, Supporting Information) biomass-derived carbon EDLC. Thus, in short, these results further confirm the promising application of the hierarchical porous structured free-standing iMBCA-E in high-performance energy storage devices.

3. Conclusion

In summary, we reported a facile and novel strategy to fabricate highly tailorable 3D hierarchical porous free-standing carbon aerogels (iMBCA-E) based on molecularly engineered alginate/pullulan semi-IPN hydrogels as the carbon source and in situ synthesized flower-like $CaCO_3$ as pore generating agent and graphitization catalyst through in situ mineralization assisted one-step activation-graphitization (iMAG). The obtained 3D binder-free iMBCA-E were tested as free-standing electrodes for high-performance capacitive electrochemical energy storage. Electrochemical investigations demonstrated that the iMBCA-E electrode fabricated by the dissolution of the biopolymers in 1 M KOH exhibited superior electrochemical properties compared to BCA-E fabricated without any KOH, with a high specific capacitance of 322 F g^{-1} at 0.5 mA cm^{-2} and excellent cyclic stability with ~104% capacitance retention over 1000 cycles at a current density of 5 mA cm^{-2}. In addition, the symmetric supercapacitor device fabricated, based on the high-performing iMBCA-E electrodes, exhibited excellent supercapacitive performance (376 F g^{-1} at 0.5 mA cm^{-2}) with a high energy density of 26 W h kg^{-1} at a power density of 4000 W kg^{-1} and superior cycling durability with 98.5% specific capacitance retained after 2000 continuous cycles. The outstanding capacitance is attributed to the unique structural features of iMBCA-E electrodes, including well-interconnected 3D porous structure, high specific surface area, high micro- and mesopore distribution, and numerous defects. The molecularly engineered alginate/pullulan semi-IPN derived free-standing hierarchical porous carbon aerogel fabricated using the iMAG approach can be extended to produce advanced free-standing biomass-derived CA-based electrodes from any ionically cross-linkable biopolymer with high structural integrity. Furthermore, the flexibility of tailoring the design using the 3DMASC method allows us to fabricate structured electrodes, thereby providing the opportunity to study the influence of size and shape on supercapacitive energy storage. Thus, 3DMASC-iMAG opens new avenues for the design and fabrication of biomass-derived free-standing 3D structured electrode materials for high-performance supercapacitors, as well as for other energy storage and environmental applications.

4. Experimental Section

Detailed information related to the synthesis of active electrodes, physicochemical characterization, and electrochemical evaluation of bifunctional electrodes towards UOR and supercapacitor application is provided in Supporting Information.

Acknowledgements

This work was financially supported by the European Research Council under the Horizon 2020 framework programme (Grant No. 772370-PHOENEEX). The authors would like to sincerely thank the Head of Characterization of DTU Nanolab, Prof. Jakob Birkedal Wagner, for his help with the TEM measurements.

Conflicts of Interest

There are no conflicts to declare.

Supporting Information

Supporting Information is available from the Wiley Online Library or from the author.

Keywords

biomass, carbon aerogel, sustainable energy materials, free-standing, supercapacitors

Received: May 5, 2022
Revised: January 3, 2023
Published online: January 14, 2023

[1] M. Zhang, A. D. Igalavithana, L. Xu, B. Sarkar, D. Hou, M. Zhang, A. Bhatnagar, W. C. Cho, Y. S. Ok, *Crit. Rev. Environ. Sci. Technol.* **2020**, *51*, 2295.
[2] D. V. Cuong, B. M. Matsagar, M. Lee, M. S. A. Hossain, Y. Yamauchi, M. Vithanage, B. Sarkar, Y. S. Ok, K. C. W. Wu, C. H. Hou, *Renew. Sustain. Energy Rev.* **2021**, *145*, 111029.
[3] R. W. Fu, Z. H. Li, Y. R. Liang, F. Li, F. Xu, D. C. Wu, *Xinxing Tan Cailiao/New Carbon Mater.* **2011**, *26*, 171.
[4] B. Rezaei, T. W. Hansen, S. S. Keller, *ACS Appl. Nano Mater.* **2022**, 5, 1808.
[5] S. Dutta, A. Bhaumik, K. C. W. Wu, *Energ. Environ. Sci.* **2014**, *7*, 3574.
[6] J. Li, R. Holze, S. Moyo, S. Wang, S. Li, T. Tang, X. Chen, *Environ. Sci. Eur.* **2021**, DOI: 10.1186/s12302-021-00527-6.

[7] Y. Li, G. Zhu, H. Huang, M. Xu, T. Lu, L. Pan, *J. Mater. Chem. A* **2019**, *7*, 9040.
[8] Y. Tao, W. Liu, Z. Li, Y. Zheng, X. Zhu, H. Wang, Y. Wang, Q. Lin, Q. Wu, Y. Pang, Z. Shen, H. Chen, *J. Colloid Interface Sci.* **2021**, *602*, 636.
[9] J. Biener, M. Stadermann, M. Suss, M. A. Worsley, M. M. Biener, K. A. Rose, T. F. Baumann, *Energ. Environ. Sci.* **2011**, *4*, 656.
[10] T. F. Baumann, M. A. Worsley, T. Y. J. Han, J. H. Satcher, *J. Non Cryst. Solids* **2008**, *354*, 3513.
[11] G. A. Yakaboylu, C. Jiang, T. Yumak, J. W. Zondlo, J. Wang, E. M. Sabolsky, *Renew. Energy* **2021**, *163*, 276.
[12] B. Wang, D. Li, M. Tang, H. Ma, Y. Gui, X. Tian, F. Quan, X. Song, Y. Xia, *J. Alloys Compd.* **2018**, *749*, 517.
[13] S. Geng, J. Wei, S. Jonasson, J. Hedlund, K. Oksman, *ACS Appl. Mater. Interfaces* **2020**, *12*, 7432.
[14] P. Li, C. Kong, Y. Shang, E. Shi, Y. Yu, W. Qian, F. Wei, J. Wei, K. Wang, H. Zhu, A. Cao, D. Wu, *Nanoscale* **2013**, *5*, 8472.
[15] Z. Gao, Y. Zhang, N. Song, X. Li, *Mater. Res. Lett.* **2017**, *5*, 69.
[16] Y. M. Fan, W. L. Song, X. Li, L. Z. Fan, *Carbon N. Y.* **2017**, *111*, 658.
[17] Y. Chang, L. Zhou, Z. Xiao, J. Liang, D. Kong, Z. Li, X. Zhang, X. Li, L. Zhi, *ChemElectroChem* **2017**, *4*, 2448.
[18] L. F. Chen, Z. H. Huang, H. W. Liang, W. T. Yao, Z. Y. Yu, S. H. Yu, *Energ. Environ. Sci.* **2013**, *6*, 3331.
[19] F. Zhang, T. Liu, G. Hou, T. Kou, L. Yue, R. Guan, Y. Li, *Nano Res.* **2016**, *9*, 2875.
[20] P. Cheng, T. Li, H. Yu, L. Zhi, Z. Liu, Z. Lei, *J. Phys. Chem. C* **2016**, *120*, 2079.
[21] H. Li, D. Yuan, C. Tang, S. Wang, J. Sun, Z. Li, T. Tang, F. Wang, H. Gong, C. He, *Carbon N. Y.* **2016**, *100*, 151.
[22] S. Zhu, P. L. Taberna, N. Zhao, P. Simon, *Electrochem. Commun.* **2018**, *96*, 6.
[23] K. Zhang, M. Liu, T. Zhang, X. Min, Z. Wang, L. Chai, Y. Shi, *J. Mater. Chem. A* **2019**, *7*, 26838.
[24] Z. Rastegar, A. Ghaemi, *Heat Mass Transf. und Stoffuebertragung* **2022**, *58*, 365.
[25] S. Li, J. Yi, X. Yu, Z. Wang, L. Wang, *Mater. Sci. Eng. C* **2020**, *110*, 110721.
[26] T. Su, L. Wu, X. Pan, C. Zhang, M. Shi, R. Gao, X. Qi, W. Dong, *J. Colloid Interface Sci.* **2019**, *542*, 253.
[27] P. Sundarrajan, P. Eswaran, A. Marimuthu, L. B. Subhadra, P. Kannaiyan, *Bull. Korean Chem. Soc.* **2012**, *33*, 3218.
[28] T. Schüler, W. Tremel, *Chem. Commun.* **2011**, *47*, 5208.
[29] B. G. Mao, D. Q. Chu, A. X. Wang, L. M. Wang, H. M. Sun, Z. Y. Zhang, X. Z. Yang, *Eur. J. Inorg. Chem.* **2013**, *2013*, 5958.
[30] P. Siqueira, É. Siqueira, A. E. de Lima, G. Siqueira, A. D. Pinzón-Garcia, A. P. Lopes, M. E. C. Segura, A. Isaac, F. V. Pereira, V. R. Botaro, *Nano* **2019**, DOI: 10.3390/nano9010078.
[31] A. W. Xu, M. Antonietti, H. Cölfen, Y. P. Fang, *Adv. Funct. Mater.* **2006**, *16*, 903.
[32] A. S. Marriott, A. J. Hunt, E. Bergström, K. Wilson, V. L. Budarin, J. Thomas-Oates, J. H. Clark, R. Brydson, *Carbon N. Y.* **2014**, *67*, 514.
[33] C. S. Gopinath, S. G. Hegde, A. V. Ramaswamy, S. Mahapatra, *Mater. Res. Bull.* **2002**, *37*, 1323.
[34] Y. Zhuang, F. Yu, H. Chen, J. Zheng, J. Ma, J. Chen, *J. Mater. Chem. A* **2016**, *4*, 10885.
[35] A. A. Edathil, P. Pal, F. Banat, *J. Environ. Chem. Eng.* **2017**, *5*, 1998.
[36] S. Dutta, J. Kim, Y. Ide, J. Ho Kim, M. S. A. Hossain, Y. Bando, Y. Yamauchi, K. C. W. Wu, *Mater. Horizons* **2017**, *4*, 522.
[37] L. Habte, N. Shiferaw, D. Mulatu, T. Thenepalli, R. Chilakala, J. W. Ahn, *Sustainability* **2019**, DOI: 10.3390/su11113196.
[38] A. I. Hussein, Z. Ab-Ghani, A. N. C. Mat, N. A. A. Ghani, A. Husein, I. A. Rahman, *Appl. Sci.* **2020**, DOI: 10.3390/app10207170.
[39] J. Li, Z. Li, X. Zhao, Y. Deng, Y. Xue, Q. Li, *J. Therm. Anal. Calorim.* **2018**, *131*, 2167.
[40] Y. Z. Yan, W. Zheng, D. Z. Huang, Z. Y. Xiao, S. S. Park, C. S. Ha, S. R. Zhai, *Microporous Mesoporous Mater.* **2020**, *293*, 109830.
[41] J. Liu, Y. Deng, X. Li, L. Wang, *ACS Sustain. Chem. Eng.* **2016**, *4*, 177.
[42] L. Xia, H. Huang, Z. Fan, D. Hu, D. Zhang, A. S. Khan, M. Usman, L. Pan, *Mater. Des.* **2019**, *182*, 108048.
[43] T. Chen, Y. Tang, Y. Qiao, Z. Liu, W. Guo, J. Song, S. Mu, S. Yu, Y. Zhao, F. Gao, *Sci. Rep.* **2016**, DOI: 10.1038/srep23289.
[44] C. Zhao, W. Wang, Z. Yu, H. Zhang, A. Wang, Y. Yang, *J. Mater. Chem.* **2010**, *20*, 976.
[45] D. Liu, B. Xu, J. Zhu, S. Tang, F. Xu, S. Li, B. Jia, G. Chen, *ACS Omega* **2020**, *5*, 11058.
[46] L. L. Zhang, Y. Gu, X. S. Zhao, *J. Mater. Chem. A* **2013**, *1*, 9395.
[47] M. Sevvila, R. Mokaya, *Energy Environ. Sci.* **1983**, *14*, 112.
[48] Y. Fang, F. Jiang, H. Liu, X. Wu, Y. Lu, *RSC Adv.* **2012**, *2*, 6562.
[49] J. Kang, S. Zhang, Z. Zhang, *Adv. Mater.* **2017**, DOI: 10.1002/adma.201700515Citations.
[50] J. Chmiola, G. Yushin, Y. Gogotsi, C. Portet, P. Simon, P. L. Taberna, *Science (80-.)* **2006**, *313*, 1760.
[51] B. Rezaei, J. Y. Pan, C. Gundlach, S. S. Keller, *Mater. Des.* **2020**, *193*, 108834.
[52] B. Pal, S. Yang, S. Ramesh, V. Thangadurai, R. Jose, *Nanoscale Adv.* **2019**, *1*, 3807.
[53] X. Ma, W. Zhou, D. Mo, Z. Wang, J. Xu, *Synth. Met.* **2015**, *203*, 98.
[54] S. Ghosh, B. Gupta, T. Mathews and A. Kamruddin, *arXiv Prepr. arXiv1603.08320*, **2016**, DOI: arXiv:1603.08320.
[55] L. Liu, X. Wang, V. Izotov, D. Havrykov, I. Koltsov, W. Han, Y. Zozulya, O. Linyucheva, V. Zahorodna, O. Gogotsi, Y. Gogotsi, *Electrochim. Acta* **2019**, *302*, 38.
[56] M. D. Stoller, R. S. Ruoff, *Energ. Environ. Sci.* **2010**, *3*, 1294.
[57] K. Sun, J. Li, H. Peng, E. Feng, G. Ma, Z. Lei, *Ionics (Kiel).* **2017**, *23*, 985.
[58] Y. Lv, L. Ding, X. Wu, N. Guo, J. Guo, S. Hou, F. Tong, D. Jia, H. Zhang, *Sci. Rep.* **2020**, DOI: 10.1038/s41598-020-64020-5.